ACS APPLIED MATERIALS & INTERFACES

Research Article

Cite This: ACS Appl. Mater. Interfaces 2018, 10, 21541−21555

www.acsami.org

Layer-by-Layer-Assembled AuNPs-Decorated First-Generation Poly(amidoamine) Dendrimer with Reduced Graphene Oxide Core as Highly Sensitive Biosensing Platform with Controllable 3D Nanoarchitecture for Rapid Voltammetric Analysis of Ultratrace DNA Hybridization

Kumarasamy Jayakumar,[*,†,∥,#] María Belén Camarada,[‡] Venkataraman Dharuman,[*,†] Rajendiran Rajesh,[§] Rengarajan Venkatesan,[§] Huangxian Ju,[∥] Mahalingam Maniraj,[⊥] Abhishek Rai,[⊥] Sudipta Roy Barman,[⊥] and Yangping wen[*,#]

[†]Department of Bioelectronics and Biosensors, Alagappa University, Karaikudi 630003, India

[‡]Centro de Nanotecnología Aplicada, Facultad de Ciencias, Universidad Mayor, Santiago, Chile

[§]Department of Chemistry, Pondicherry University, Pondicherry 6050114, India

[∥]State Key Laboratory of Analytical Chemistry for Life Science, Department of Chemistry, Nanjing University, Nanjing 210023, P. R. China

[⊥]UGC-DAE Consortium for Scientific Research, Khandwa Road, Indore 452001, Madhya Pradesh, India

[#]Institute of Functional Materials and Agricultural Applied Chemistry, Jiangxi Agricultural University, Nanchang 330045, P. R. China

Supporting Information

ABSTRACT: The structure and electrochemical properties of layer-by-layer-assembled gold nanoparticles (AuNPs)-decorated first-generation (G1) poly(amidoamine) dendrimer (PD) with reduced graphene oxide (rGO) core as a highly sensitive and label-free biosensing platform with a controllable three-dimensional (3D) nanoarchitecture for the rapid voltammetric analysis of DNA hybridization at ultratrace levels were characterized. Mercaptopropinoic acid (MPA) was self-assembled onto Au substrate, then GG1PD formed by the covalent functionalization between the amino terminals of G1PD and carboxyl terminals of rGO was covalently linked onto MPA, and finally AuNPs were decorated onto GG1PD by strong physicochemical interaction between AuNPs and −OH of rGO in GG1PD, which was characterized through different techniques and confirmed by computational calculation. This 3D controllable thin-film electrode was optimized and evaluated using $[Fe(CN)_6]^{3-/4-}$ as the redox probe and employed to covalently immobilize thiol-functionalized single-stranded DNA as biorecognition element to form the DNA nanobiosensor, which achieved fast, ultrasensitive, and high-selective differential pulse voltammetric analysis of DNA hybridization in a linear range from 1×10^{-6} to 1×10^{-13} g m^{-1} with a low detection limit of 9.07×10^{-14} g m^{-1}. This work will open a new pathway for the controllable 3D nanoarchitecture of the layer-by-layer-assembled metal nanoparticles-functionalized lower-generation PD with two-dimensional layered nanomaterials as cores that can be employed as ultrasensitive and label-free nanobiodevices for the fast diagnosis of specific genome diseases in the field of biomedicine.

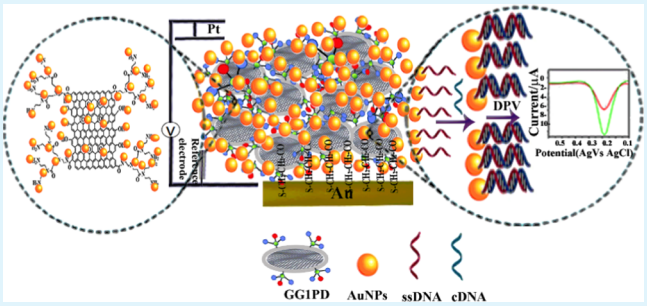

KEYWORDS: *DNA biosensor, layer-by-layer assembly, three-dimensional nanoarchitecture, poly(amidoamine) dendrimer, gold nanoparticles, graphene*

1. INTRODUCTION

DNA biosensors have been intensively employed for infectious disease assay, pathogen recognition, cancer diagnosis, environmental monitoring, and others.[1,2] Ultrasensitive analysis of DNA hybridization is a low-cost, significant-specific, and high-sensitive technique, which has attracted fascinating attention for the diagnosis of specific gene diseases in the field of biomedicine.[1,2] Electrochemical biosensing techniques usually offer highly effective methods for the hybridization analysis of DNA,[3−5,2] but DNA hybridization biosensing based on electrochemical impedance spectroscopy (EIS) is time-consuming and may deteriorate the sensing performance.

Received: February 24, 2018
Accepted: June 5, 2018
Published: June 5, 2018

DOI: 10.1021/acsami.8b03236
ACS Appl. Mater. Interfaces 2018, 10, 21541−21555

Scheme 1. Systematic Scheme of the LBL-Assembled AuNPs-Decorated G1PD with rGO Core as a Highly Sensitive and Label-free Biosensing Platform with Controllable 3D Nanoarchitecture for Rapid DPV Analysis of DNA Hybridization at Ultratrace Levels

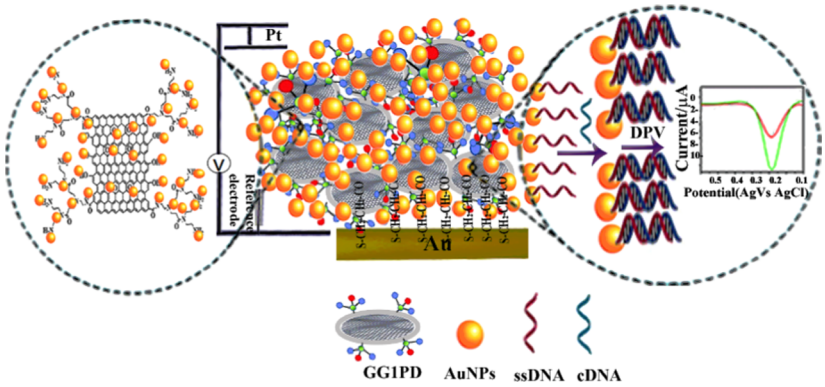

Difference pulse voltammetry (DPV) is one of the preferred methods due to its high sensitivity, extraordinary resolution, ultratrace analysis, and fast response.

Nowadays, substrate electrodes assembled/modified by various nanomaterials as promising nanobiosensing platforms have been explored/exploited for the amplified detection of DNA to overcome safety problems as well as poor sensitivity and stability.[3−5] Graphene with high surface area can improve the capacity of electron transport and exhibits excellent biocompatibility.[6] Therefore, many approaches have been used to develop graphene-based biomedical devices,[6−10] with the aim of lowering the limit of detection (LOD) and improving stability toward various biosensors.[10−14] Graphene nanohybrids have been used to design label-free DNA biosensing devices, showing high discriminative performance of electrochemical DNA biosensor. Guo et al. used in situ probe techniques to design an azophloxine covalently functionalized graphene,[15] which is an excellent selective DNA biosensor. Moreover, polymer-functionalized graphene decorated with gold nanoparticles (AuNPs) were used to improve the sensing performance like electrocatalytic ability, selectivity, and sensitivity. Yuan et al. reported 3,4,9,10-perylenetetracarboxylic acid covalently functionalized graphene for the synthesis of AuNPs due to the negatively charged COOH and amine-terminated ionic liquid.[16] More importantly, nanoparticles exhibited great uniformity on the graphene surface and thus the capture DNA probe could be easily functionalized by strong electrostatic interactions, resulting in excellent sensitive detection of DNA hybridization. Chen et al. fabricated a device based on AuNPs-functionalized nitrogen-doped graphene hybrids, improving catalytic behavior, selectivity, and sensitivity toward sensing of DNA hybridization.[17]

Poly(amidoamine) (PAMAM) dendrimer (PD), a very interesting commercially available macromolecule with highly dendritic structure and well-defined three-dimensional (3D) hyperbranched polymeric nanoarchitectures, is highly flexible and capable of forming multiple interaction sites between most of their branch ends and functional materials. Lower-generation PDs with various cores make them extraordinary matrixes for the recent development of biosensors due to their controllable size and structure, high mechanical and chemical stabilities, modifiable surface functionalities, recognition and binding of biomolecules, enhanced target-capturing ability, excellent sensitivity, hydrophilicity, monodispersity, stability, specificity, and reusability of biosensors.[18] Liu et al. reported disulfide cross-linked low-generation PD with high transfection efficacy, low cytotoxicity, and low cost,[19] which are efficient alternatives to the high-generation PD with high cost and serious cytotoxicity in gene delivery. More interestingly, the lower-generation PD with various nanomaterials as cores has more catalytic active sites because of high surface-to-volume ratio, good structural stability, and excellent improvement of DNA sensing via the increasing charge-transfer properties. Zhu et al. investigated the second-generation (G2) PD with multiwalled carbon nanotube core as the tether for DNA biosensor,[20] which provides many amino groups to increase the surface binding of DNA and increases the sensitivity of the impedimetric biosensor for the target DNA. Metal nanoparticles-decorated PD as a signal amplification element for the highly selective and sensitive detection of DNA hybridization has also been reported.[21] AuNPs-decorated lower-generation PD composites have opened fractal structure that could be more stable and active as a catalytic site. Tang et al. designed a AuNPs-decorated PD, which provided biocompatible immobilization and a promising immunosensing platform for highly sensitive electrochemical analysis of small molecules and the detection of food safety.[22] Dietrich et al. mentioned that G2PD could control the size of AuNPs better, leading to excellent catalytic activity and stable structure, thereby enhancing biosensing performance.[23]

In this work, we focused on the construction, characterization, and optimization of a controllable 3D nanoarchitecture based on layer-by-layer (LBL)-assembled AuNPs-decorated first-generation (G1) PD with reduced graphene oxide (rGO) as core covalently functionalized with mercaptopropinoic acid (MPA) self-assembled nanolayer onto the surface of gold (Au) substrate (Scheme 1), which was employed as highly sensitive and label-free nanobiosensing platform for the rapid DPV analysis of DNA hybridization at ultratrace levels. This study will focus on the controllable fabrication of open and porous structure through LBL-assembled methods and the characterization of controllable 3D nanoachitecture based on G1PD with a nanomaterial as core.

2. EXPERIMENTAL SECTION

2.1. Materials and Reagents. MPA and graphite powder (50 nm) were purchased from Loba Chemie Pvt. Ltd., Mumbai, India. Thiolated short-chain 27 mer synthetic oligonucleotides with high-performance liquid chromatography purification were all synthesized by MWG Biotech, Ebersberg, Germany. Their base sequences are as follows: capture single-stranded DNA (ssDNA) is 5′-HS-$(CH_2)_6$-CGA

DOI: 10.1021/acsami.8b03236
ACS Appl. Mater. Interfaces 2018, 10, 21541−21555

T CTG TTT TAT GTA GGG TTA GGT CA-3′ (I), cDNA is 5′-TG ACC TAA CCC TAC ATA AAA CAG-3′ (II), ncDNA is 5′-TAC CAT TCT CAT CTC TGA AAA CTT CCG-3′ (III), smDNA is 5′-TGA CCT AAC CCC ACA TAA AAC AG -3′ (IV). Graphite powders were purchased from Loba Chemie Pvt. Ltd., Mumbai, India. The other chemicals, such as H_2SO_4, NaOH, $HAuCl_4{\cdot}3H_2O$, MPA, 1-ethyl-3-(3-dimethylaminopropyl)carbodiimide (EDC), $K_4[Fe(CN)_6]$ $K_3[Fe(CN)_6]$ methylene blue (MB), trisodium citrate, ethylene diamine, methylacrylate, and hydrogen peroxide, were obtained from Sigma-Aldrich (St. Louis, MO). All chemicals were of analytical grade, pH of the solutions was adjusted using 0.1 M H_2SO_4 and 0.5 M NaOH, and all solutions were prepared using double-distilled water.

2.2. Instruments. Electrochemical measurements were made using a CH Instruments potentiostat (model 650D, 440B, CH Instruments Inc.) and a three-electrode system comprising polycrystalline gold electrode as working electrode (1.6 mm diameter, 99.9% purity), platinum wire as counter electrode, and Ag/AgCl as reference electrode. The preparation of the polycrystalline gold electrode involves a first immersion into piranha solution containing H_2SO_4 and H_2O_2 mixture at 7:3 ratio at room temperature and an immersion time of 2 min. Platinum wire electrode was polished with alumina (1 μm) powder, washed with double-distilled water, and sonicated for 5 min. The morphology analysis was performed using a scanning electron microscope (Hitachi-S-4300, Germany). Atomic force microscope scans were obtained using APE Research-model no: A100SGS with tapping mode. Transmission electron microscopy (TEM) images were used to analyze the layer size and crystalline structure (Tecnai G2-20 instrument from FET Company, Hillsboro). Attenuated total reflection-Fourier transform infrared (ATR-FTIR) spectra were recorded using a PerkinElmer Nicolet ISI instrument in the frequency range of 4000−400 cm^{-1}. Solid-state NMR spectra were obtained using a Varian Mercury 300 Plus 300 MHz spectrometer. The probe had switchable high-frequency and high-broad-band-frequency-range NMR (^{13}C, ^{31}P, ^{15}N) and might be spun up to maximum 5 kHz at magic angle. Positive and negative ion spectra were acquired (peaks m/z, 0−1000) using a time-of-flight secondary ion mass spectrometry (TOF-SIMS) spectrometer (Tof-SIMS V, ION GmbH, Munster, Germany). The Surface Lab 6.0 software from ION-TOF was used to analyze peaks. X-ray photoelectron spectroscopy (XPS) measurements were carried out using a Phoibos 100 electron energy analyzer from Specs GmbH, Germany. X-ray diffraction (X'Pert PRO PANalytical) analysis was performed with Cu Kα radiation as a source and a potential of 20 kV was applied. The sample was scanned at the range of 10−80° with 1 s per step. Surface-enhanced Raman spectroscopy (SERS) measurements were made using a confocal Raman microscope (CRM 200, CRM-α −300s, WITec, GmbH, Germany, with Ar ion laser (514.5 nm)). The spectral range was from 10× to 100× with a scan range of 100 × 100 μm^2. EIS results were modeled through the simple Randel's equivalent circuit expression $[R_s(QCPE(R_{ct}W))]$ (Scheme 2), where R_s is the solution resistance, R_{ct} is the charge-transfer resistance, W is the Warburg impedance, and QCPE is the constant phase element (CPE), given by the equation $Z(\omega) = 1/QCPE(j\omega)n$, where $\omega = 2\pi f$ is the angular frequency, with f, the frequency and n, the dimensional CPE promoter-signified frequency dependent on the degree of the surface roughness of a phase homogeneity layer of the transducer surface.

Scheme 2. Simple Randel's Equivalent Circuit Expression of $[R_s(QCPE(R_{ct}W))]$

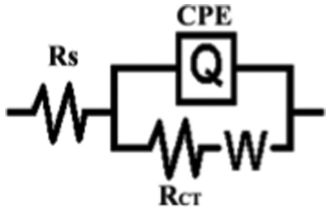

2.3. Fabrication of 3D LDL AuNPs/GG1PD/MPA/Au. The preparation of GO from graphite followed the Hummers and Offeman method.[24] The synthesis and characterization of GG1PD was described in our previous work.[25] The synthesis of AuNPs was achieved by referencing the method proposed by Frens et al.[26] The MPA was formed onto the Au surface by dip-coating method, and both MPA concentrations (1, 2, 3, and 4 mM) and immersion times (30, 60, 90, and 120 min) were optimized for the self-assembled architecture of MPA. Then, the GG1PD layer was immobilized onto the surface of the MPA self-assembled monolayer by drop-coating method. In this process, the peptide linkage of the acid to the amine functional group was achieved by 5 mM EDC, which activated the MPA self-assembled monolayer for 4 h to form *O*-acylisourea. Then, the amide linkage was promoted with the terminal amine functional groups of 1 μM GG1PD with an immersion time of 8 h at room temperature. Finally, the electrode was washed with phosphate-buffered saline (PBS) (pH = 7.4) and dried at room temperature. The fresh AuNPs were deposited onto the surface of AuNPs/GG1PD/MPA/Au at 4 °C at different incubation times by drop-coating method. To improve the catalytic activity, the size of AuNPs was controlled to regulate the specific detection of the DNA hybridization. Electrochemical behaviors of all electrodes were measured in 0.01 M PBS (pH 7.4) containing 1 mM $[Fe(CN)_6]^{3-/4-}$.

2.4. Immobilization and Hybridization of DNA. A small volume (5 μL) of 1 μM thiol-functionalized ssDNA in 1 M NaCl was immobilized onto 3D LDL AuNPs/GG1PD/MPA by drop-coating method and incubated for 2 h at 4 °C to form probe I. The probe I was then washed with PBS to remove unbounded thiol-functionalized ssDNA and dried at room temperature. After that, the probe I was hybridized with 5 μL of 1 μM cDNA for 2 h to form probe II, then rinsed with 10 mM PBS to remove the nonhybridized cDNA, and dried at room temperature. Similarly, 5 μL of 1 μM ncDNA or smDNA was used to obtain probe III and probe IV under similar experimental conditions. Their surface behaviors were measured intermittently in PBS buffer containing 1 mM $[Fe(CN)_6]^{3-/4-}$ using cyclic voltammetry (CV) and EIS. The EIS and DPV techniques were used for studying target variation.

2.5. Computational Details. With the aim of studying the most stable site of coordination between AuNPs and the GG1PD system, computational calculations were performed. Because of the size of the system, for energy calculations involving AuNPs, it was necessary to introduce a smaller structure consisting of a graphene surface functionalized with hydroxyl and epoxy moieties, with four branches derived from G0PD, as depicted in Figure 1. This structure was identified as GG0PD. The geometries of GG1PD and GG0PD were fully optimized at the density functional theory (DFT) level using the Gaussian 0927 computational package. The oxidation ratios inserted in the structures were in accordance with the experimental characterization. AuNPs were represented by a small eight-atom cluster (Au). Full geometry optimization of complexion reactions between GG0PD and Au_8 was calculated using the Becke's three-parameter nonlocal hybrid exchange potential with the nonlocal correlation functional of Lee, Yang, and Parr (B3LYP)[27−29] without any symmetry restriction. The triple-ζ 6-31G basis set was set for light atoms (C, H, O, and N) along with a relativistic effective core potential basis set with pseudopotentials for the gold atoms, LANL2DZ.[30] The tight SCF convergence criterion (10^{-8} au) was used in all calculations. Charge distribution of the intermolecular interactions was calculated using the natural population analysis (NPA) method,[31] as implemented in Gaussian 09. Interaction energy (E_{int}) is defined as the energy difference between the complex and constituent monomers. Computation of this quantity with finite basis sets introduces an error known as basis set superposition error (BSSE) because different numbers of basic functions are used to describe the complex and the monomers for the same basis set. BSSE-corrected interaction energies were computed using the Boys−Bernardi counterpoise correction scheme.[32]

DOI: 10.1021/acsami.8b03236
ACS Appl. Mater. Interfaces 2018, 10, 21541−21555

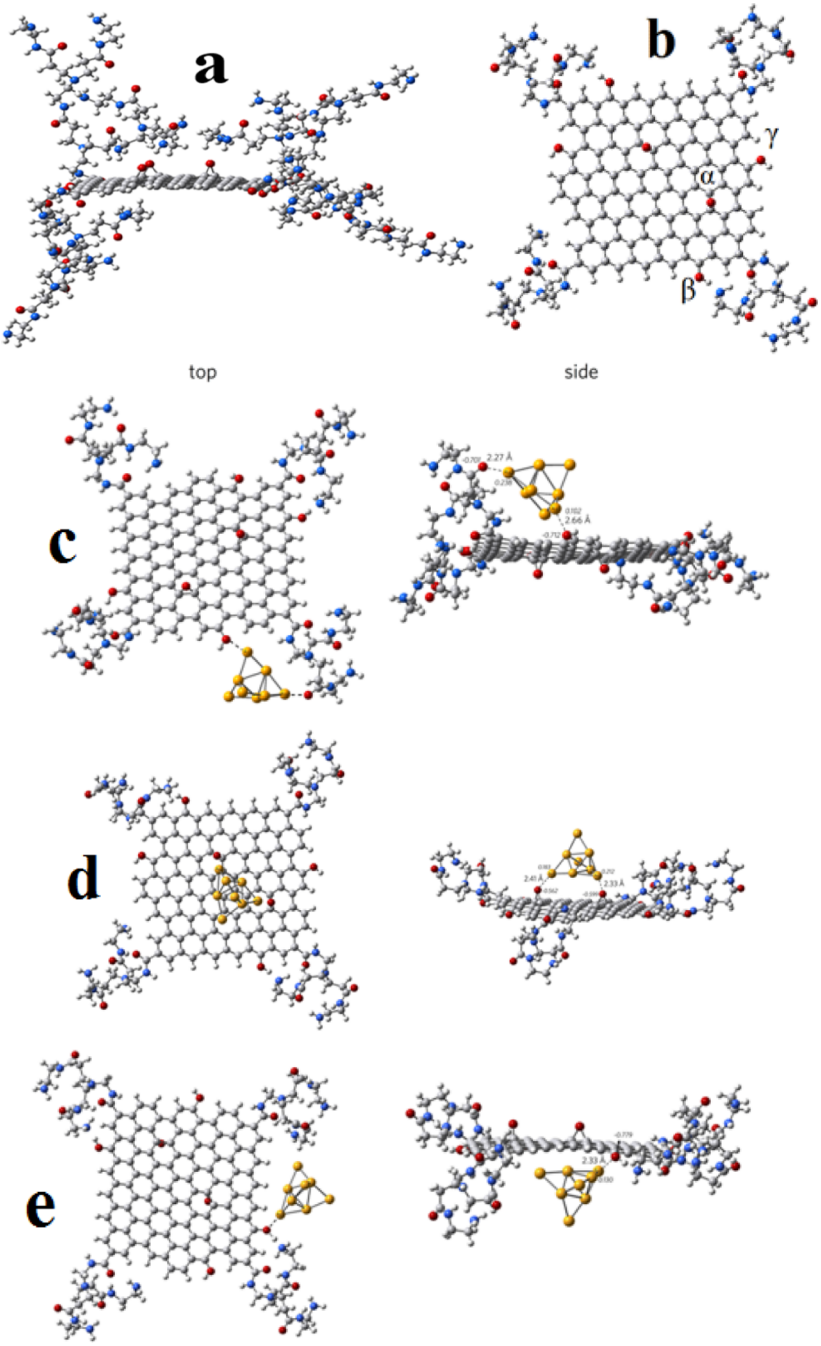

Figure 1. Optimized structures of GG1PD (a) and GG0PD (b) with the three possible coordination sites considered at B3LYP/6-31G. Top and side views of the ground-state geometry of the Au_8−GG0PD complex optimized at site (c), (d), and (e) at the B3LYP/6-31G//LANL2DZ level. AuNP charges (au) for selected atoms are displayed in italic. The bond lengths are expressed in angstrom.

3. RESULTS AND DISCUSSION

3.1. Morphology and Structure of 3D LBL AuNPs/GG1PD/MPA. The ATR-FTIR spectrum (Figure S-1a) of the MPA monolayer self-assembled onto Au substrate (MPA/Au) indicates that CH_2 peaks of MPA on a gold substrate appear at 2928 and 2856 cm^{-1} (no peaks of any organic species appear at the unmodified Au surface). The asymmetric and symmetric stretching vibrations of $-CH_2$ of its alkane appear at 2919 and 2850 cm^{-1}, respectively. The location of its CH_2 stretch vibration gives more information about lateral interactions between *n*-alkyl chains.[33] However, the most important feature is the C═O stretching band of the acid end group of MPA, which appears at 1635 cm^{-1},[33−35] usually referred to an acid group that participates in the process of the hydrogen bond. The absorption band at 1045 cm^{-1} is attributed to the C−O−H vibration of MPA.[36] In addition, acid groups of MPA involved in the hydrogen bond present a band at ∼1453 cm^{-1} (COO−, symmetry). The surface morphology of GG1PD/MPA/Au is a smooth crumpled layer and the folded layer with the exposed plane edges, which is assigned to the modification of rGO with G1PD (Figure 2a), while AuNPs/GG1PD/MPA/Au reveals that spherical sizes were randomly distributed on the GG1PD surface (Figure 2b). ATR-FTIR spectra (Figure 2c) of GG1PD/MPA/AuNPs and AuNPs/GG1PD/MPA/Au reveal

DOI: 10.1021/acsami.8b03236
ACS Appl. Mater. Interfaces 2018, 10, 21541−21555

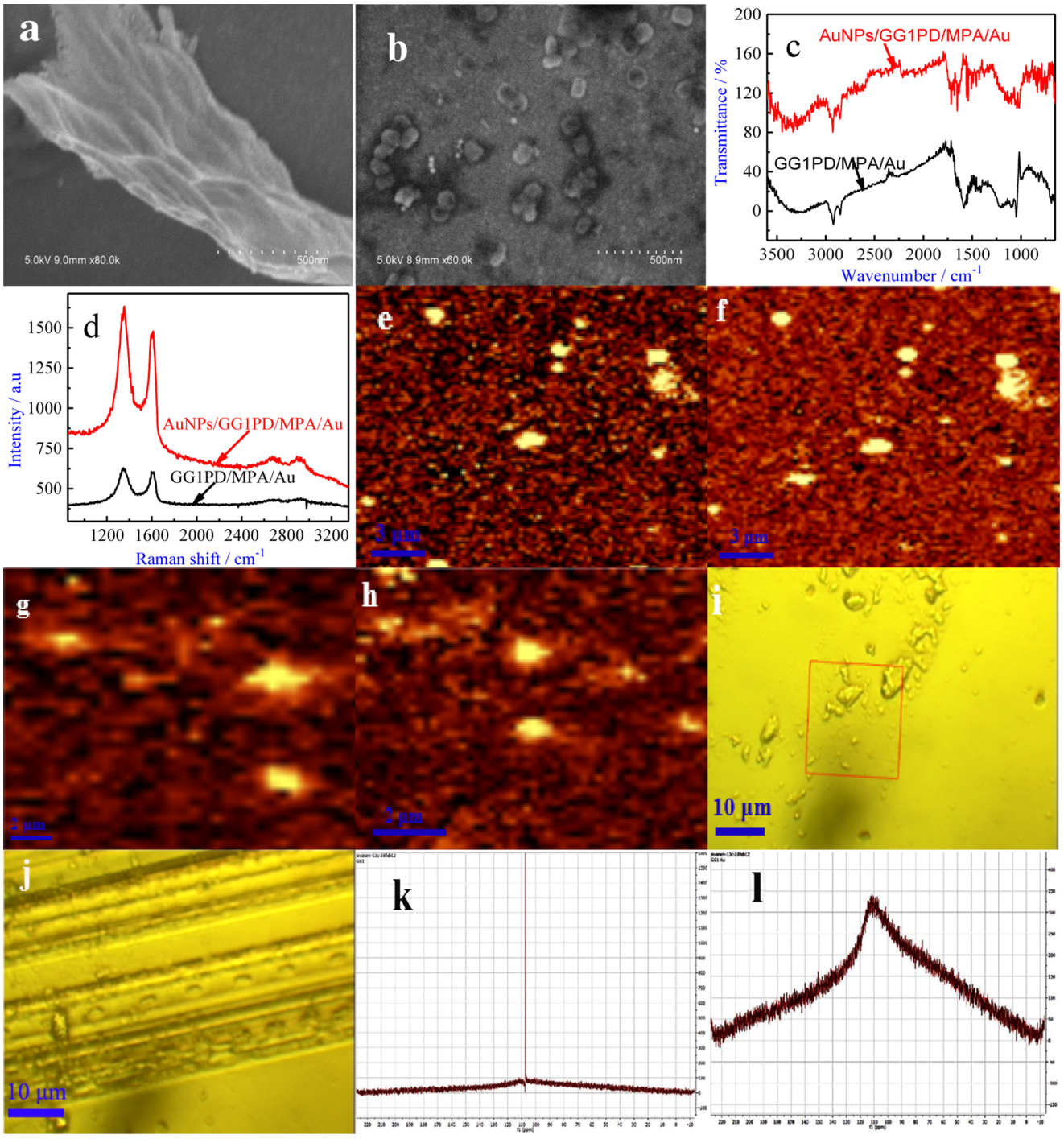

Figure 2. Scanning electron microscopy (a, b), ATR-FTIR (c), Raman (d), SERS Raman (e, f), Raman optical (g, h), and SERS optical images at 2911 cm^{-1} (i, j). ^{13}C solid-state NMR ($^{13}CSSNMR$) spectra (k, l) of NMR spectrum of both GG1PD/MPA/Au and AuNPs/GG1PD/MPA/Au.

that bands at 1655, 1596, and 3325 cm^{-1} are characteristic peaks of amide and amine groups, respectively. Strong peaks are detected at 2919 and 2850 cm^{-1} from the asymmetric and symmetric stretching modes of methylene groups in the MPA layer (Figure S-1a), respectively. The peaks at 1059 and 1446 cm^{-1} are assigned to the presence of phenolic (C−OH) hydroxyl groups and their deformation, respectively. AuNPs/GG1PD/MPA/Au has a high intense peak corresponding to the C−OH at 1039 cm^{-1} due to AuNPs coordination to the C−O.[36] Raman spectroscopy is often used to analyze the crystalline nature of graphene structures. SERS spectra of GO (Figure S-1b) and GG1PD and AuNPs/GG1PD (Figure 2a) show D, G, 2D, and D + D′ or D + G bands at 1350, 1607, 2683, and 2911 cm^{-1}, respectively. The D band appears from the disordered stacking of graphene layers and atomic defects at edges. The G band arises from the first-order Raman scattering process of the in-plane vibration of sp^2-bonded carbon atoms. The 2D band originates from the double-resonance Raman process of two phonons and are closely related to the band structure of graphene layers; also, they do not require defects for activation. The appearance of the 2D peak is treated as a fingerprint of crystalline carbon materials. The D + D′ or D +

DOI: 10.1021/acsami.8b03236
ACS Appl. Mater. Interfaces 2018, 10, 21541−21555

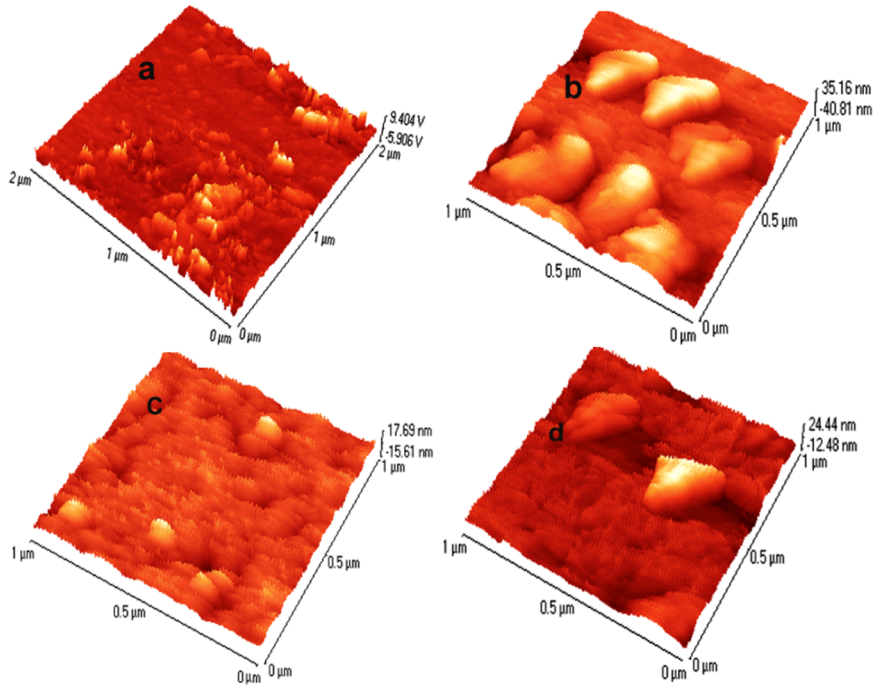

Figure 3. AFM images of (a) bare Au, (b) GG1PD/MPA/Au, (c) AuNPs/GG1PD/MPA/Au, and (d) ssDNA/AuNPs/GG1PD/MPA/Au.

G band is related to the presence of convention-activated structural defects, which have an accessibility of shape, position, and relatively intensity ratios and are characteristics of layers of graphene structures.[37] The transition from bulk graphite to nanocrystalline graphite and vice versa produce pronounced effects in Raman spectra.[38] Furthermore, the intensity of the D-band is related to structural disorders in the sp^2 lattice and the I_D/I_G ratio is indicative of covalent defect site concentration and characterizes the degree of covalent functionalization.[39] The band intensities are normalized with respect to the G band intensity for further analysis and comparison. The I_D/I_G ratio of the prepared AuNPs/GG1PD decreases (0.77) compared to the GG1PD (1.04) and GO (1.23). The higher I_D/I_G ratio of GG1PD indicates higher structural disorder resulting from edge defects after GG1PD functionalization. It may be noted that GG1PD is attached to carboxyl groups of GO, confirming that PDs are attached to GO surface and retain sp^2 carbons. Thus, I_D/I_G ratios of both GO and GG1PD are unaltered. The deposition of AuNPs increases Raman intensities of both D and G bands. The decreasing I_D/I_G ratio (0.77) of AuNPs/GG1PD suggests highly decreased structural disorder due to changes in flatness or roughness of GG1PD sandwiched between MPA and AuNPs (Figure 2e–h).

Raman spectral behaviors can be used to estimate the crystallite size (La, nm) of the sp^2-hybridized carbon using eq S-1 (see Supporting Information).[39] The La values are 29.23 nm for GO, 19.48 nm for GG1PD, and 26.54 nm for AuNPs/GG1PD. Optical images of GG1PD and AuNPs/GG1PD (Figure 2i,j) exhibit intensities of spectral lines from 1300 to 1800 cm^{-1} due to a decrease in the disorder of structural defects and pulling of the crystalline structure. Moreover, AuNPs can also be deposited on the bottom lying of the gold transducer, filling the defect and decreasing the disorder, which further increases the La. ^{13}C solid-state NMR ($^{13}CSSNMR$) spectra present a peak at 108 ppm (Figure 2k), which belongs to the unhybridized graphite sp^2 carbon network of GG1PD.[40] The appearance of a broad resonance at 50–150 ppm (Figure 2j) confirms the restoration of sp^2 carbons and the formation of GO.[41] In contrast, a broad peak of AuNP-functionalized GG1PD shows a blue shift at 110 ppm (Figure 2j) due to the decreasing structural disorder.[23,42] Great changes are clearly observed in the morphologies of atomic force microscopy (AFM) images between the bare Au surface (Figure 3a) and films-modified Au surfaces (Figure 3c,d). After 120 min immersion, the MPA layer shows small spherelike objects of 5.8 nm height (Figure S-2).

This results in a highly ordered profile of two-dimensional structures. The unmodified electrode presents an increasing thin-film size of 15.8 nm, which relates to the lesser dense structure. The GG1PD molecule (Figure 3b) appears as a densely packed platelet-like film on the MPA layer with a porous structure and an incremented surface height (35.16 nm). The modification of AuNPs toward GG1PD smoothens the film (Figure 3c), decreases the porous nature, reduces redox peak currents (both I_{pa} and I_{pc} (Figure S-3a)), increases changes in charge-transfer resistances (ΔR_{ct}, Figure S-3b) of the dense film, and regulates the surface roughness via decreasing the active surface on the height AuNPs/GG1PD film using $[Fe(CN)_6]^{3-/4-}$. The average surface height of AuNPs/GG1PD decreases to 17.69 nm. When the capture ssDNA is immobilized on the AuNPs/GG1PD/MPA/Au (Figure 3d), the surface became rougher and the average surface height increased from 17.69 to 24.44 nm, indicating the effective attachment of the ssDNA to the surface of AuNPs/GG1PD. Obviously, the single-stranded DNA (ssDNA)-functionalized AuNPs with a height difference of 5–7 nm reveal that the more dense package nanostructure influences the emulous reactions between them and the electrode surface. The AFM height profile image confirms the assembly of DNA molecules onto the AuNPs surface with strong binding, resulting in a highly precise and predictable bionanostructure. High-resolution TEM (HRTEM) reveals that the PD has been exfoliated on edges of graphene, forming a wrinkle or folding structure (Figure 4b) with potential application in biomedical devices. The

DOI: 10.1021/acsami.8b03236
ACS Appl. Mater. Interfaces 2018, 10, 21541–21555

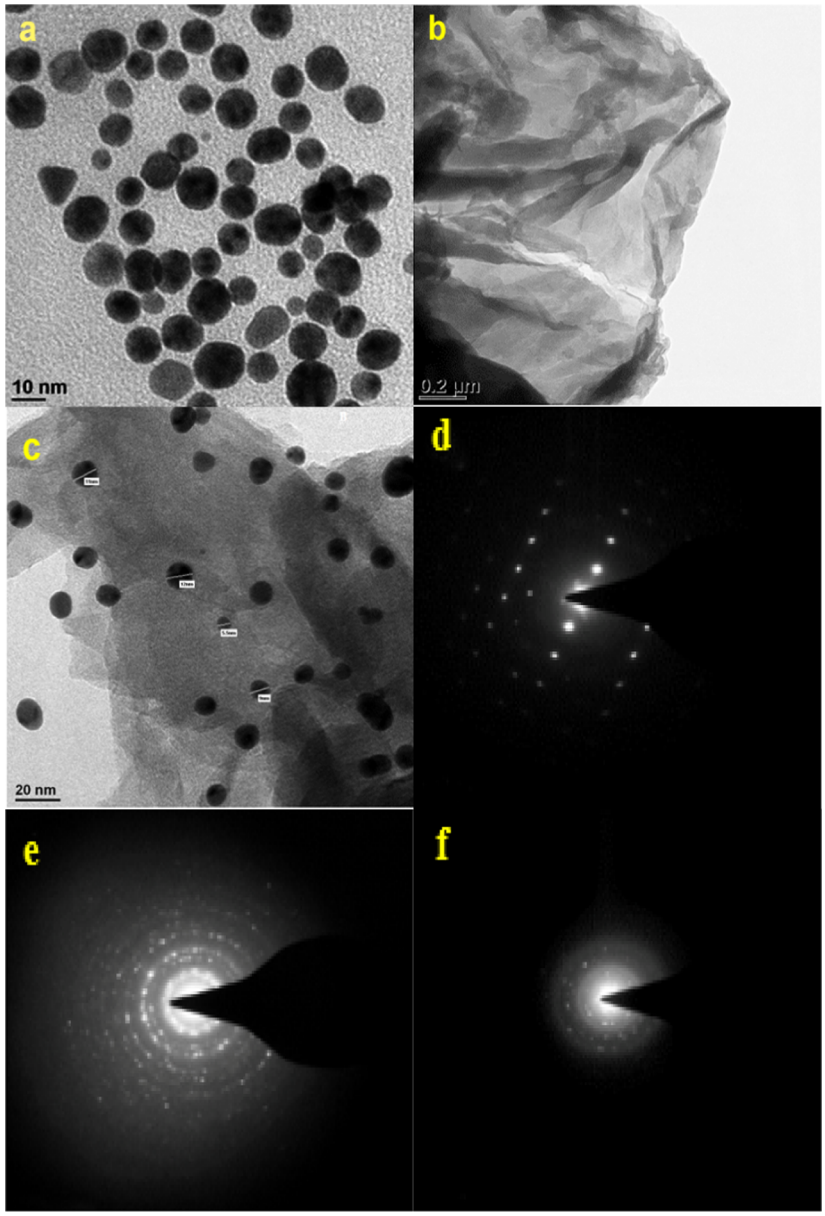

Figure 4. HRTEM and SAED patterns of AuNPs (a, d) GG1PD (b, e), and AuNPs/GG1PD (c, f).

comparison between AuNPs (Figure 4a,d) and GG1PD (Figure 4b) clearly reveals that spherical AuNPs with different sizes are deposited at the edges of graphene, where they are attached (Figure 4c). Then, the particle size increases to 63 ± 5 nm due to the larger mobility of electron charge and the reduction of physical absorption of AuNPs on GG1PD. However, the reduction of GO core plays a significant role in assembling AuNPs on the oxyfunctional groups, acting as a nucleation site for the growth of AuNPs. In addition, the undefined selected area electron diffraction (SAED) pattern reveals poor crystalline nature of the carbon in GG1PD (Figure 4e), whereas AuNPs/GG1PD shows a clear SAED pattern for (100) type carbon with higher intensity (Figure 4f). UV spectra of different materials are presented in Figure S-4a. AuNPs (curve c) show a peak at 520 nm due to the gold plasmon resonance effect, and solutions show a weak additional absorption band at 250 nm.[35] The GO gives a single absorption band at 257 nm resulting from the $\pi-\pi^*$ transition of the aromatic C−C network. The AuNPs/GG1PD show two absorption maxima at 520 and 245 nm. This is similar to the uncomplexed AuNPs with less intensity. However, the GG1PD only shows absorption maximum at 272 nm, which is 15 nm red-shifted from the GO peak (257 nm).[36] The red shift at 272 nm is consistent with the increase in hydrophobic nature and confirms the functionalization of GO with G1PD.[36] The strong physiochemical interaction of AuNPs/GG1PD (curve b) implies that peak intensities decrease at 250 and 520 nm in the UV−visible spectra of GG1PD.

TOF-SIMS spectra (Figure 5) are obtained to verify chemical states of nitrogen in the GG1PD-functionalized surface. Cleavage structures of graphene carbon ring obtained from 1 to 200 m/z of AuNPs/GG1PD are C_x^- (x = 1, 2, 3,...), C_xH^+, $C_xH_2^+$, C_x^-, and C_xH. Xie et al. investigated the graphene structure of PD nanocomposite using TOF-SIMS.[37] They reported the cleavage of the graphene major ring structure, observing C_x^- (x = 1, 2, 3...), C_xH^+, $C_xH_2^+$, C_x^-, and C_xH^-, which could be successfully integrated to decompose the nature of PD toward various temperatures to investigate the stiffness

DOI: 10.1021/acsami.8b03236
ACS Appl. Mater. Interfaces 2018, 10, 21541−21555

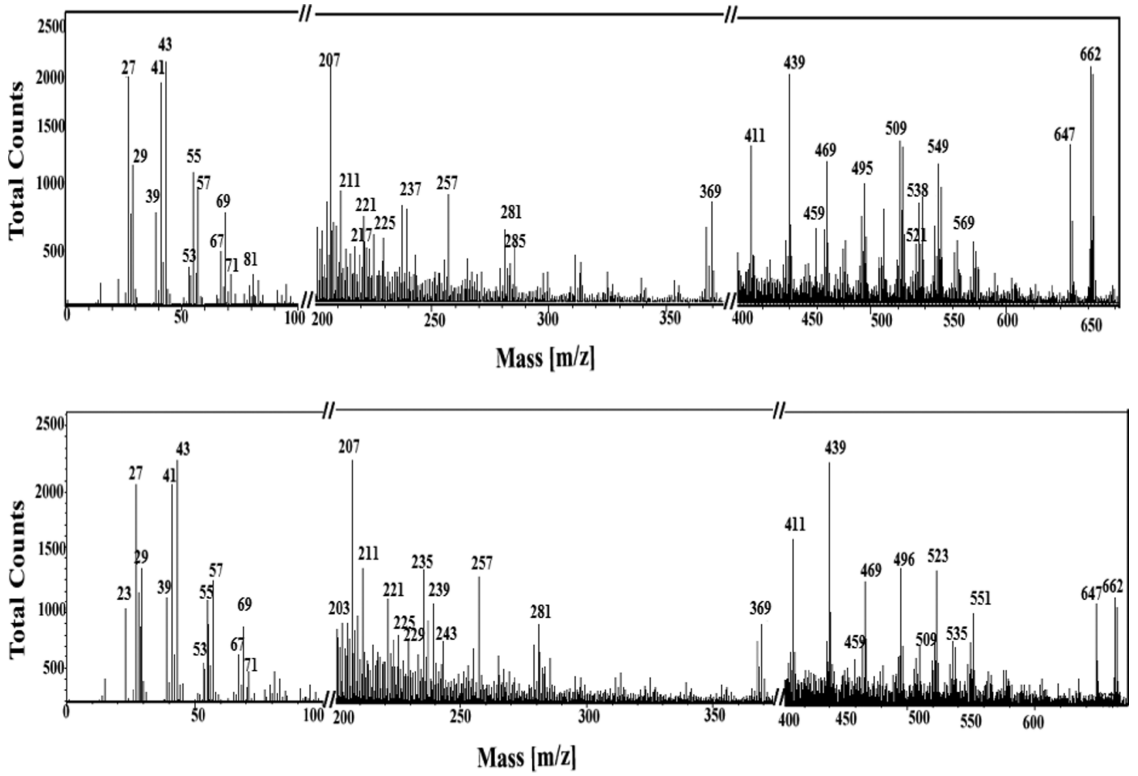

Figure 5. TOF-SIMS spectra of AuNPs/GG1PD immobilized on Si/SiO_2 measured in the upper spectrum range from m/z 200 to 1000.

of graphene layers. As Figure 5 shows, graphene carbon anion peaks are strongly observed from negative modes C_2^-, C_3^-, C_4^-, C_5^-, C_6^-, C_7^-, C_8^-, C_9^-, C_{10}^-, C_{11}^-, C_{12}^-, C_{13}^-, C_{14}^-, C_{15}^-, C_{16}^-, and C_{17}^- corresponding to m/z 24.0, 36.0, 48.0, 60.0, 72.0, 84.0, 96.0, 108.0, 20.0, 132.0, 144.0, 156.0, 168.0, 180.0, 192.0, and 204.0. The amide nitrogens are also detected in the form of $CH_2ON^+(O{=}C{-}NH_2)$, $-C_3H_6NO^{2-}$, $(-CH_2CH_2-CO-NH_2)_2^-$, $C_{22}H_{39}O_4N_{52}^-$, and $C_{40}H_{50}O_4N_{52}^-$ at m/z = 43, 72, 439, and 662 eV, respectively. Comparison among relative intensities of these nitrogen compounds reveals the covalent functionalization of GG1PD, confirming the formation of MPA. The interaction of AuNPs with the GG1PD surface results in lower peak intensities for amine and amide groups.

Characteristic peaks of XPS images of gold (Au $4f_{7/2}$, 84.06 eV), sulfur atom (S 2p, 162.5 eV), carbon (C 1s, 284.5 eV), nitrogen (N 1s, 399 eV), and oxygen (O 1s, 531 eV) suggest the presence of the respective functional groups (Figure 6a). The presence of their particular elements, compositions, and chemical environments on the surface of the sensor can be identified by deconvolution processes of the XPS peak of the particular element. The deconvoluted S 2p spectra of both GG1PD (Figure 6b) and AuNPs/GG1PD (Figure 6c) layers attached onto the MPA/Au demonstrate that GG1PD shows only one peak (Figure 6b), whereas AuNPs/GG1PD shows two peaks (Figure 5c) at 161.9 and 163.5 eV.[34] Since MPA is used as the anchoring layer, both layers show S 2p peak at 162 eV. The S 2p peak at 161.9 eV is attributed to gold−sulfur bond (Au−S), and the second peak at 163.5 eV is up-shifted by 1.45 eV with respect to Au−S species and is assigned to the free thiols (S−H) onto the gold substrate.[34] This can be because a small amount of the alkanethiols is not covalently bound to the substrate, but trapped in the monolayer defects, such as pinholes and collapsed sites, or physically adsorbed on the surface. The XPS image of AuNPs/GG1PD has a splitting ratio difference of 1.12 eV. C 1s spectra of GG1PD (Figure 6d) and AuNPs/GG1PD (Figure 6e) indicate that binding energies of different carbons are observed at 284.5 eV (graphitic C═C species), 285.3 eV (C−C), 286.25 eV (C−N), and 288.0 eV (N−C═O).[40,43] GG1PD decorated with AuNPs shows lower peak intensities and increased atomic percentages (Figure 6e).[23,39] It may be noted that the single layer of graphene on the Au-coated substrate has a binding energy of 284.4 eV, and the suspended single layer graphene has a higher binding energy of 284.8 eV.[44] The C 1s peak of GG1PD is observed at 284.4 eV, which is lower than that of GG1PD−AuNPs observed at 284.8 eV. This confirms the presence of a single layer of graphene on the Au-coated substrate. N 1s spectra of GG1PD (Figure 6f) and AuNPs/GG1PD (Figure 6g) reveal the presence of nitrogen in three different chemical environments, with peaks located at 394.05, 396.1, and 399.9 eV. It has been tacitly assumed that the N 1s binding energy is around 396−397 eV. This peak for the nitrogen appears in the substituted systems. The binding energy decreases to ∼399.90 eV for the chemisorbed molecular species.[45] This confirms the presence of a single layer of graphene on the Au-coated substrate. The nitrogen in anionic states, as is generally believed, shows a binding energy of ∼394 eV. The slightly higher binding energy of AuNPs/GG1PD may be related to the existence of a resonance structure, with a strong physical interaction between AuNPs and nitrogen atom in GG1PD.[40,43] Collectively, these data confirm the efficient covalent attachment of GG1PD using EDC coupling reagent on the MPA monolayer pretethered on Au chip. The O 1s peaks obtained for GG1PD (Figure 6h) and AuNPs/GG1PD (Figure 6i) films were deconvoluted into two peaks with binding energy values of 532.5 and 533.5 eV, corresponding to the doubly bonded oxygen and singly bonded oxygen from alcohols, ethers, and

DOI: 10.1021/acsami.8b03236
ACS Appl. Mater. Interfaces 2018, 10, 21541−21555

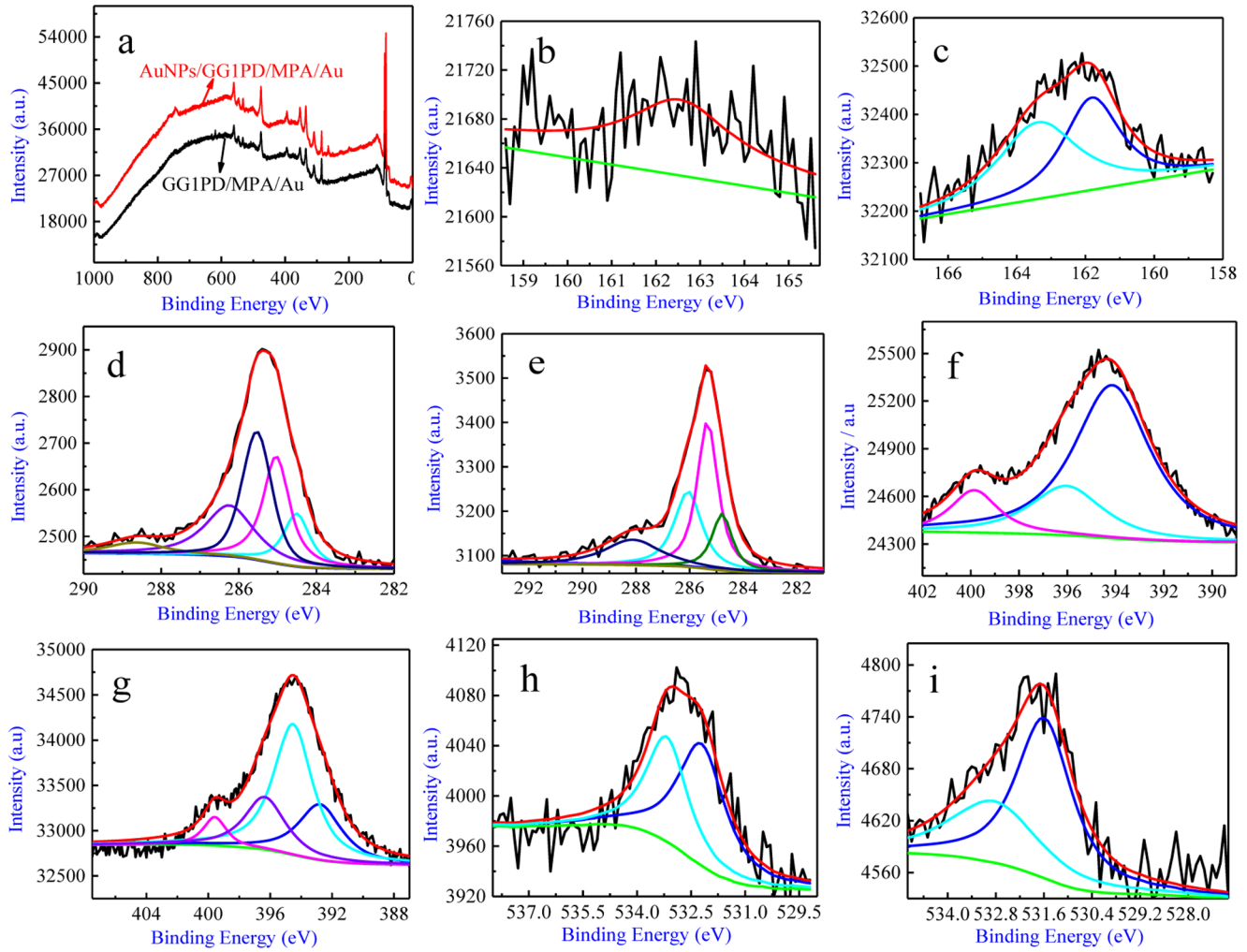

Figure 6. Survey XPS images (a), S 2p (b, c), C 1s (d, e), N 1s (f, g), and O 1s (h, i) of both GG1PD/MPA/Au and AuNPs/GG1PD/MPA/Au using Alg Kα source with excitation energy of 1486 eV.

epoxies.[17,43] The binding energy was shifted to a higher value (0.4 eV) due to the incorporation of AuNPs on rGO edge (C−OH or C−O−C groups). Figure S-4b exhibits a doublet corresponding to Au $4f_{5/2}$ (87.4 eV) and Au $4f_{7/2}$ (83.45 eV), relating to spin−orbit coupling.[17,40,43] The values of binding energies are consistent with the presence of different Au^{+} states in AuNPs. The strong electrostatic interaction between GG1PD and AuNPs has a slight effect on binding energies of Au peaks (Figure S-4b).

3.2. DFT Calculations. The isolated GG1PD structure was fully optimized at the B3LYP/6-31G level. PD could interact with functional groups on the surface of the rGO core (Figure 1a), generating a packed structure with curve shape. A smaller generation for the GG1PD system was built because of the size of this structure and the high computational costs associated with its optimization. Smaller zero generation PD was functionalized with rGO core (GG0PD, Figure 1b). This structure was used as reference for the calculation of E_{int}. Several initial conformations were tested to search for alternative local minima. Figure 1b shows the optimized GG0PD geometry calculated at the B3LYP/6-31G level of theory. Internal hydrogen bonds were established between amide groups, specifically the oxygen atom of the carbonyl site belonging to the graphene oxide core and terminal amines from different branches contribute to the system stabilization, as well as interactions between hydroxyl moieties at the edge of the graphene layer and amino terminal groups. G0PD has some potential coordination sites with high electron density, where a gold cluster could be able to attach and generate a complex.[46] Starting geometries of Au_8−GG0PD complexes for the optimization were generated by placing the Au_8 cluster near the electron-rich sites of the structure. The Au_8 cluster was optimized at the LANL2DZ level.

Three different coordination sites were considered (Figure 1b): Au_8 interacting with (α) the surface of graphene and −O− moieties, (β) a hydroxyl (−OH) group and one branch of the dendrimer, and (γ) a −OH group on the edge of the graphene layer. Table S-1 summarizes the E_{int}, distances between the gold cluster and the anchor oxygen atom, and charge for three optimized complexes. BSSE-corrected binding energies indicate that the most stable Au_8−GG1PD complex corresponds to structure (β).

Figure 1C shows this optimized system, in which bond lengths, natural charges at selected atomic sites, and atomic numbering schemes are depicted. Other two optimized geometries are available in Figure 1C,D. The system (β) has two oxygen atoms acting as anchoring sites: the hydroxyl group placed at the edge of the graphene layer and a carbonyl group belonging to the dendrimer branch. The complex (α) has also a double coordination to oxygen atoms of epoxy moieties on

DOI: 10.1021/acsami.8b03236
ACS Appl. Mater. Interfaces 2018, 10, 21541−21555

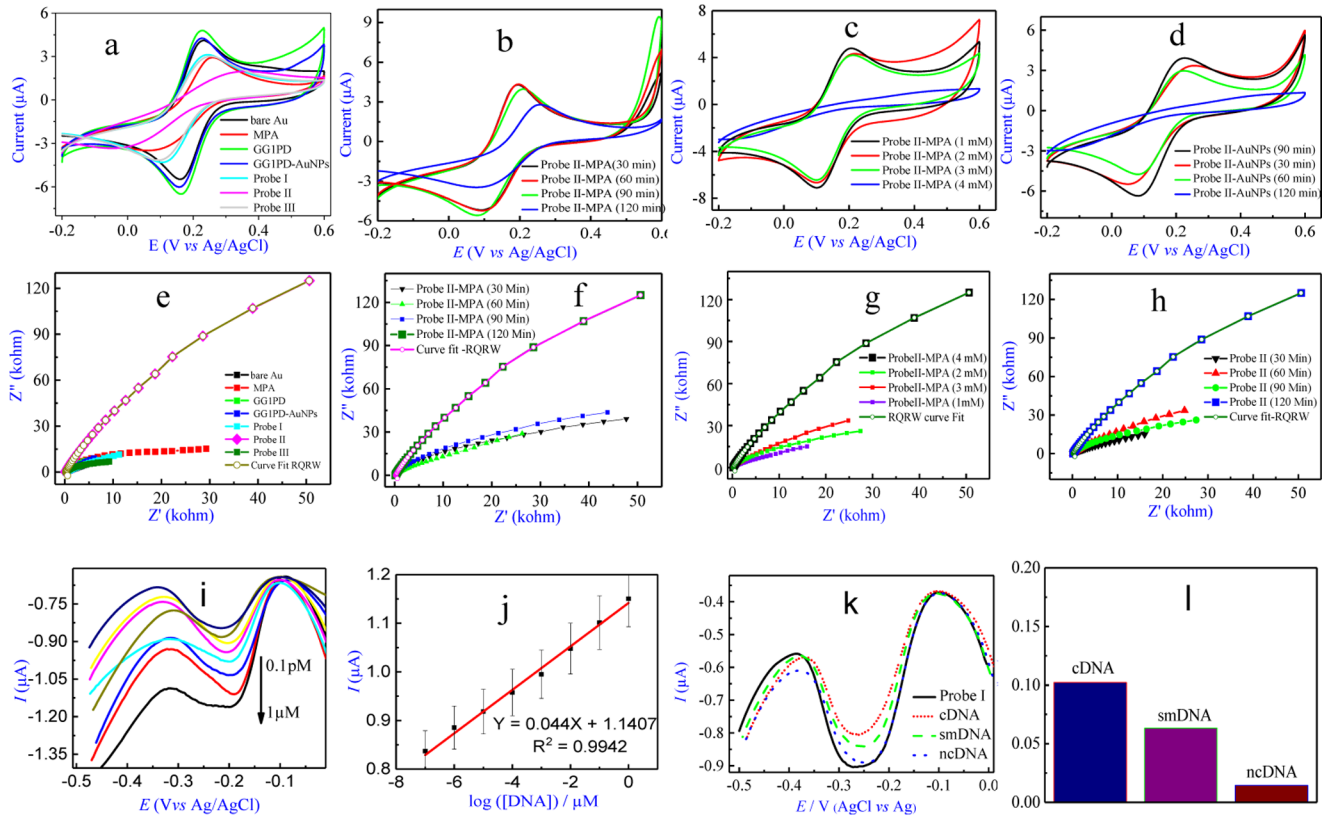

Figure 7. CVs (a) and Nyquist plots (e) of different modified electrodes in PBS (pH 7.4) containing 1 mM $[Fe(CN)_6]^{3-/4-}$. CVs and Nyquist plots of MPA with immersion times of 30, 60, 90, and 120 min (b, f) and concentrations of 1, 2, 3, and 4 mM (c, g), AuNPs (d), and probe II (h) with incubation times of 30, 60, 90, and 120 min. DPVs (i) of probe I after hybridization with different concentrations (1 μM, 0.1 μM, 0.01 μM, 1 nM, 0.1 nM, 0.01 nM, 1 pM, 0.1 pM) of cDNA for reduction signals of MB in PBS (pH 7.4), and calibration curves (j) for the linear relationship between reduction peak current of MB and the logarithm of DNA concentration. Selectivity (k) of probe I with 1 nm concentration of cDNA, smDNA, and ncDNA, and ΔI_{pa} of DPV (l) in PBS (pH 7.4).

graphene, which is 8.8 kcal mol^{-1} more unstable than the system (β). On the other hand, when the total NPA charge of the gold cluster (Δqcluster) is analyzed, and it can be noted that the highest amount of charge was transferred to the complex (β), approximately 30% more than the amount transferred from the ligand to (α).

This evidence is related to the fact that electron densities belonging to the oxygen atoms at epoxy groups are delocalized throughout the conjugated system. Lone pairs are not totally available and generate weaker interaction with gold atoms. Therefore, the electron shared by lone-pair orbits of these atoms and the gold 5d and 6s orbitals play an important role in stabilization. The complex (γ) is the only structure with single coordination to an oxygen atom and has the lowest E_{int}. Nevertheless, this value is quite close to system (α) that has a double coordination. Moreover, the complex (γ) presents the most negative Δqcluster value of whole series, indicating that the highest electron density was transferred from the ligand to the gold cluster. According to these results, the interaction of the gold cluster (Au_8) with −OH sites is comparable energetically to the epoxy sites of the GG0PD, but has a greater strength. The interaction of gold atoms with hydroxyl groups is reinforced and stabilized with the coordination to PAMAM branches. Results obtained through DFT calculations indicate that AuNPs will tend to grow close to hydroxyl groups and dendrimer branches more than epoxy sites, which is in accordance with experimental results, where AuNPs are covalently functionalized to −OH side groups of the rGO core of GG1PD. In this way, nanoparticles are excellently stabilized by the dendritic structure, increasing the electrocatalytic performance.

3.3. Electrochemical Properties and Application in DNA Nanobiosensor. The MPA/Au has smaller redox peak current (Figure 7a) and higher R_{ct} compared to bare Au substrate (Figure 7e). These are explained by an insulating behavior of MPA with more electronegative groups (COO^-) on the electrode interface, which produce the electrostatic repulsion between COO^- and $[Fe(CN)_6]^{3-/4-}$. The MPA has a higher peak-to-peak separation between the reduction and oxidation peaks of $[Fe(CN)_6]^{3-/4-}$ (ΔE_p) than bare Au (Figure 7a). It can be concluded that MPA has a blocking effect toward $[Fe(CN)_6]^{3-/4-}$ owing to its non-low conductivity. GG1PD/MPA/Au has a markedly increasing redox peak current (Figure 7a) and a decreasing R_{ct} (Figure 7e) compared to MPA/Au because of the high specific surface area, absorption capacity, and electrical conductivity of G1PD with rGO core. AuNPs/GG1PD/MPA/Au has a decreasing redox peak current (Figure 7a) and an increasing R_{ct} (Figure 7e) compared to GG1PD/MPA/Au because of the presence of negatively charged citrate ions adsorbed on AuNPs, which led to the electrostatic repulsion between the negatively charged AuNPs and $[Fe(CN)_6]^{3-/4-}$.

There is an obvious decrease in redox peak currents (Figure 7b) and a dramatical increase of ΔE_p (Figure 7b) and ΔR_{ct} (Figure 7f) at the immersion time of 120 min due to the presence of more carboxylic amount of GG1PD, further

DOI: 10.1021/acsami.8b03236
ACS Appl. Mater. Interfaces 2018, 10, 21541−21555

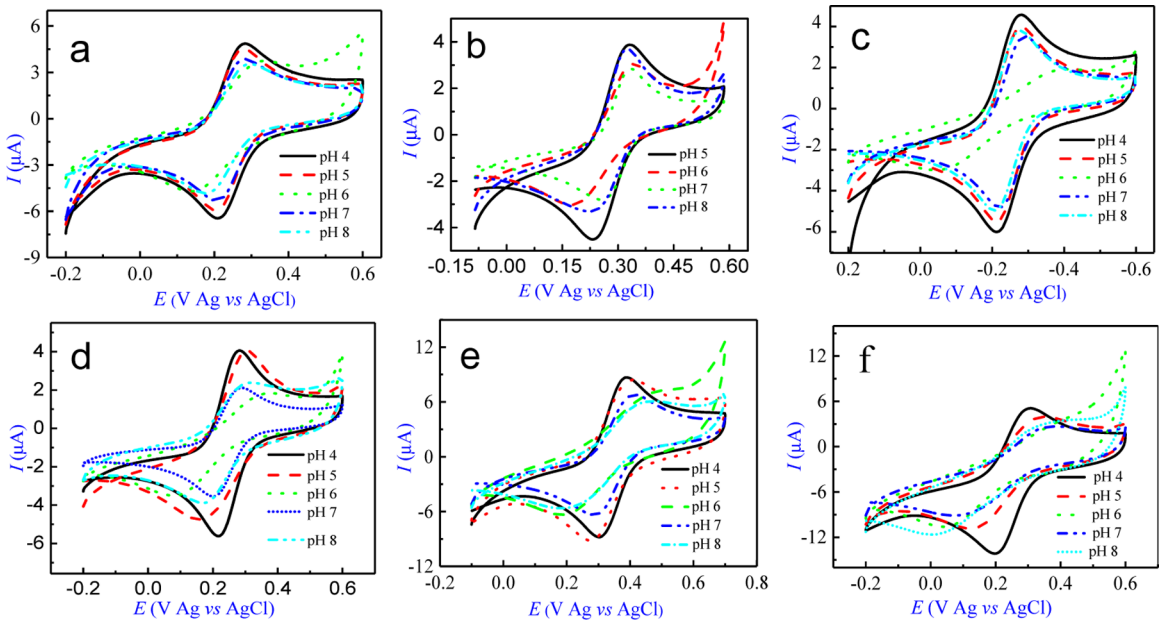

Figure 8. Effect of pH at bare Au (a), MPA/Au (b), GG1PD/MPA/Au (c), AuNPs/GG1PD/MPA/Au (d), probe I (e), and probe II (f) using CVs.

resulting in the deposition of large quantities of AuNPs, better immobilization of thiol-functionalized ssDNA, and the final hybridization of many cDNA. Phosphate groups increase the electrostatic repulsion between negative charges of DNA and negative charges of $[Fe(CN)_6]^{3-/4-}$, even the blocking effect of insulating materials like MPA and DNA.

The increasing concentration of MPA (Figure 7c,g) results in the increase of both ΔE_p (Figure 7c) and ΔR_{ct} (Figure 7g) and the decrease of both I_{pa} and I_{pc} owing to the presence of more MPA, which ultimately generates a blocking effect due to the electrostatic repulsion or the insulating behavior of the as-fabricated electrode. AuNPs with incubation times of 30, 60, 90, and 120 min obviously influence redox peak currents and ΔE_p (Figure 7d). A distinct decrease in redox peak currents (Figure 7d) and a visible increase of ΔE_p (Figure 7d) at 120 min incubation time are assigned to the presence of large quantities of AuNPs, which is very favorable for the immobilization of higher amounts of ssDNA and the subsequent hybridization of many target cDNA. This produces an insulating behavior of DNA on the transducer interface because of their electrostatic repulsion between negative charges of both $[Fe(CN)_6]^{3-/4-}$ and phosphates. Probe II with different incubation times (30, 60, 90, and 120 min) also influences ΔR_{ct} (Figure 7h). A remarkable increase of ΔE_p reveals that the presence of a greater quantity of negatively charged phosphate backbone densities in target cDNA increases the electrostatic repulsion force against negative charges of the redox probe. The 3D open fractal structure of GG1PD has a large specific surface area, which can extensively increase the electrode surface area of GG1PD/MPA/Au, improve the electron transfer, and decrease the R_{ct} compared to the bare Au (Figure 7a). The electrochemical behavior of the GG1PD-modified electrode is attributed to the lone-pair electron on the C−N groups of GG1PD that can catalyze the redox reaction of $[Fe(CN)_6]^{3-/4-}$. Meanwhile, the AuNPs-functionalized GG1PD exhibits lower peak currents and lower resistance (R_{ct}). It can be stated that AuNPs produce a synergic effect with GG1PD, resulting in the composite-modified electrode with an enhanced electrocatalytic activity. The optimal and controllable particle size and shape of AuNPs are attributed to the stabilization of the metal nanoparticles through the binding to various functional groups on GG1PD surface, such as oxygen functional groups of graphene core hydroxide, epoxies, as well as terminal amine ($-NH_2$) functional groups or interior functional groups (C−N). Increasing densities of AuNPs indicates a high catalytic activity because of the small size of particles on GG1PD, which improves the conductivity and decreases the resistance (Figure 7d). The size and structure of AuNPs are important factors for the selectivity and sensitivity of the DNA hybridization. The size of AuNPs affects the surface volume ratio and improves the catalytic activity of GG1PD nanocomposite. The analysis reveals that particles are uniformly deposited on a small area of the electrode and enhance charge transfers of redox probe. The immersion time of 120 min increases the catalytic activity because of the oxygen functional group sides that change the charge capacitance, increase the efficiency of electron charge transfer, and decrease R_{ct}. Finally, the functionalization of AuNPs onto the GG1PD surface heals the structure of the graphene, resulting in a tunable electronic structure, which has promised to enhance the electron charge-transfer mechanism of the interaction particle due to the increasing crystalline layer structure.

The thickness of the film is inversely proportional to the CPE and directly proportional to the dielectric constant. The increasing thickness of the MPA layer with higher concentration has an insulating effect. The adhesion of acid functional groups is a relative permittivity constant values (0.11×10^{-6}, 0.13×10^{-6}, 0.16×10^{-6}, and 0.21×10^{-6}), which can be related to an orientation of alkyl chains and ionizable acid groups on the surface (Figure 7g). The immersion time regulates the surface coverage of MPA molecules and changes the nonspecifically absorption ability of biological molecules. Longer immersion times (120 min) decrease surface roughness, creating a highly efficient uniform molecular package, with controllable capabilities of the 3D structure. With the extension of immersion times, the increasing thickness of the MPA layer also has an insulating effect, which results in higher degree of integrity of the structure, with lower gauche defects and denser

DOI: 10.1021/acsami.8b03236
ACS Appl. Mater. Interfaces 2018, 10, 21541−21555

packed surface. The increased charge density of the MPA layer with higher thickness has an insulating effect, reflecting the increased surface polarizability with greater dielectric constant values (6.23×10^{-6}, 6.44×10^{-6}, 6.97×10^{-6}, and 7.85×10^{-6} F cm^{-2}) because the steric hindrance has significantly controlled the redox probe for the electrode surface (Figure 7h).

The pH effects of different modified electrodes were investigated (Figure 8), and all redox peak currents decreased with the increase of pH values, especially the ΔE_p values increase with the increase of pH values (Figure 8b,d–f), which is most likely because electronegative groups like phosphate group and carboxylic group increased the electrostatic repulsion force. All response currents were minimum at pH 6.0 when DNA was not immobilized onto the surface of modified electrodes (Figure 8a–d), while response current is minimum at pH 8.0 when DNA was modified onto the surface of the fabricated electrode, but response current is minimum at pH 7 when DNA hybridization was carried out (Figure S-5a–e). Biological macromolecules usually exist in neutral environments, and current responses of probe I before and after hybridization were obviously affected by both strong acid and alkali due to the damage of the helical structure and the denature of DNA. Therefore, pH 7.4 was selected for follow experiments. The incubation time also influences current responses of probe I before and after hybridization. Response currents were minimum at about 60 min before hybridization and approximately 90 min after hybridization, which could generate a negatively charged interface to electrostatically repel redox probe indicators $[Fe(CN)_6]^{3-/4-}$. Hence, the optimal incubation time of probe I was about 60 min before hybridization and approximately 90 min after hybridization (Figure S-5a,b). Binding energies of probe I at different incubation times (30, 60, 90, and 120 min) were calculated as 22, 46, 18, and 20 mV, respectively. Moreover, binding energies of probe II at different incubation times (30, 60, 90, and 120 min) were calculated as 12, 17, 6 and 15 mV, respectively. We concluded the stronger bonding of the electrode surface on capture probe DNA, ssDNA (60 min) and dsDNA (90 min), which can be an excellent uniform orientation structure to improve the DNA hybridization.

The electroactive surface area (A) values, which are different from the geometric ones of different electrodes, are measured by peak current versus square root of scan rates (ν) (Figure S-6a–f). The values of different electrodes are calculated by CVs (Figure S-6) using eq S-2 (see Supporting Information). The A value of bare Au electrode is 4.47×10^{-6} cm^2 s^{-1}, whereas MPA-modified Au electrode has a lower active surface area with a value of 1.26×10^{-6} cm^2 s^{-1}, indicating that MPA has a blocking effect toward $[Fe(CN)_6]^{3-/4-}$. GG1PD increases the active surface area (6.12×10^{-6} cm^2 s^{-1}) and thus improves the electron transfer. This behavior is related to the single layer of graphene on the flexible cavity of the hydrophobic PD layer. This composite increases the surface volume ratio and enhances the electrocatalytic activity between the graphene core and the cavity of the internal and terminal amine groups. Finally, the diffusion layer thickness of AuNPs/GG1PD leads to higher peak currents due to an increase in the particle size and active surface area with an A value of 7.35×10^{-6} cm^2 s^{-1}. Besides, as the microscopic area increases due to the presence of AuNPs, the available catalytic active sites increase.

The average surface coverage values (Γ, eq S-3, see Supporting Information) of ssDNA at different incubation times (30, 60, 90, and 120 min) of AuNPs on the surface of as-fabricated electrode are 1.10×10^{-10}, 1.25×10^{-10}, 1.47×10^{-10}, and 7.14×10^{-10} mol cm^2, respectively. The larger Γ value at 120 min suggests that there is more absorbed ssDNA due to the deposition of upper quantities of AuNPs, which enhances the amplification of DNA hybridization. Moreover, the hybridization of cDNA improves negative charge densities (ΔE_p 300 mV) because of the presence of more phosphate links on the electrode surface that increases the electrostatic repulsion force on $[Fe(CN)_6]^{3-/4-}$. The growth of AuNPs on GG1PD surface is regulated and reached a saturation of nanoparticles. The coordination of AuNPs to functional groups of GG1PD, especially −OH moieties in rGO core, enhances charge capacitance, chemical stability, and catalytic activity and further improves the DNA hybridization sensing.

CVs of different modified electrodes at different ν were investigated in PBS containing 1 mM $[Fe(CN)_6]^{3-/4-}$ at scan rates ranging from 10 to 400 mV s^{-1}. All oxidation peak potentials shifted toward more positive potentials, all reduction peak potentials shifted toward more negative potentials with increasing ν (Figure S-7), and curves of all peak current versus $\nu^{1/2}$ increased linearly with $\nu^{1/2}$ (Figure S7), all of which suggested that electrode reactions were diffusion-controlled electrode processes.[47] Besides, plots of $\log I_{pa}$ versus $\log \nu$ yielded slope values between 0.5 and 1 (Figure S8). The slope value is greater than the theoretical value of 0.5 for diffusion-controlled process while smaller than the theoretical value of 1 for the adsorption-controlled electrode process, suggesting that the redox peak derives not only from the molecules adsorbed on the surface of different modified electrodes before oxidation–reduction but also from the ones reaching the electrode surface by diffusion.[48,49] In addition, I_{pa} and I_{pc} of different modified electrodes almost overlapped ($I_{pa}/I_{pc} \approx 1.0$), indicating good reversible redox behaviors and high structural stability.

To determine the interfacial electrokinetics of probe II at incubation times of 30, 60, 90, and 120 min (Figure 7h), the values of standard heterogeneous charge-transfer rate (K_a^0, eq S-4, see Supporting Information) are calculated to be 1.19×10^{-6}, 7.26×10^{-7}, 1.60×10^{-7}, and 2.12×10^{-8} cm s^{-1}, respectively. It is clearly observed that the K_a^0 value decreases with the increase of DNA hybridization because of the formation of double helical structure on the surface. The increasing impedance on the electrode surface is largely attributed to the phosphate-blocking effects, producing an insulating behavior of more target DNA on the transducer interface, increasing charge resistance with the higher negative charge (phosphate groups in target DNA), which produces electrostatic repulsion of $[Fe(CN)_6]^{3-/4-}$. As Figure 7h shows, high concentrations (incubation time of 120 min) of cDNA enhance DNA hybridization.

The thiol-functionalized ssDNA is immobilized onto the surface of AuNPs/GG1PD/MPA/Au to form probe I, which results in decreasing redox peak currents (Figure 7a), increasing ΔE_p (Figure 7a), and increasing ΔR_{ct} (Figure 7e) due to the introduction of nonconducting ssDNA and the electrostatic repulsion between the negative charge of phosphate backbones of probe I and $[Fe(CN)_6]^{3-/4-}$, suggesting that the thiol-functionalized ssDNA is successfully linked onto the surface of AuNPs/GG1PD/MPA/Au. The probe II is formed when probe I is used to hybridize with the corresponding cDNA, which further observably increases both ΔE_p (Figure 7a) and R_{ct} (Figure 7e) and markedly decreases redox peak currents

DOI: 10.1021/acsami.8b03236
ACS Appl. Mater. Interfaces 2018, 10, 21541–21555

(Figure 7a), indicating further increase in the nonelectroconductivity of dsDNA on the electrode surface and further enhancement in the electrostatic repulsion between negative charges of phosphate backbone of dsDNA-modified electrode and $[Fe(CN)_6]^{3-/4-}$. However, probe III is formed when probe I is used to hybridize with ncDNA under the same experimental conditions, and negligible changes in redox peak currents (Figure 7a), ΔE_p (Figure 7a), and R_{ct} (Figure 7e) due to the absence of pairing sequence suggest the development of a highly selective device for the electrochemical detection of DNA.

The highly sensitive DPV is used to study the concentration effect of target DNA in the presence of dsDNA containing MB that has strong affinity for dsDNA than for ssDNA (Figure 7i). Extensive research has been reported on DNA biosensing applications of MB as an intercalator.[50] Figure 7i shows the DPV for the reduction signal of MB with probe I after hybridization with target dsDNA (probe II). The highest MB reduction signal is observed with probe I alone, as MB has a strong affinity for free guanine bases and hence the greatest amount of MB accumulation occurs at this surface.[51] An obvious decrease in the voltammetric peak current is observed after duplex formation (Figure 7i), as the interaction between MB and guanine residues of the probe has been prevented by hybrid formation on the electrode surface. A voltammetric signal is still expected even when the entire probe DNA has hybridized to a duplex, as MB can also act as an intercalator.[52] However, the suppression of the MB signal after hybridization indicates that the voltammetric signal is small compared to signal from direct interaction with the guanine bases due to the intercalation. The effective discrimination against single-base mismatch is also studied. The presence of smDNA (probe III) significantly decreases voltammetric signal compared to ncDNA (Figure 7k,l). This difference indicates that the complete hybridization is not accomplished due to the base mismatch, which demonstrates that the MB interacts strongly with DNA molecules.[52]

The proposed DNA nanobiosensor shows a dynamic linear range from 1×10^{-13} to 1×10^{-6} M, and its corresponding linear regression equation is represented as I_p (μA) = 0.044 log C (μM) + 1.1407 with a correlation coefficient of 0.9942 (Figure 7j). The limit of detection (LOD) was calculated using eq S-5 as 9.07×10^{-14} M. In comparison to DNA nanobiosensors based on graphene or metal nanoparticle nanocomposites in previous reports (Table S-2), the presented DNA nanobiosensor has much wider linear range and lower LOD, which implies that the proposed DNA nanobiosensor is a potential electrochemical biosensing platform for DNA-sensing application in different fields.[1,53−56] Moreover, 1 nM concentrations result in the observable current response presented by DPV measurements, indicating an ultrasensitive AuNPs/GG1PD surface for the rapid detection of DNA hybridization (Figure 7k), suggesting the formation of larger clusters like AuNPs on the GG1PD surface, which varies with measurements of each concentration. Hence, AuNPs may nonspecifically absorb the ssDNA, which results in improper orientation and reduces the hybridization efficiency. On this basis, the controlled orientation of ssDNA on the AuNPs−graphene nanocomposites is essential to improve the sensitivity and renewability of DNA biosensor for practical applications.

4. CONCLUSIONS

LBL-assembled AuNPs-decorated GG1PD onto MPA-modified Au substrate as an ultrasensitive and label-free nanobiosensing platform with a controllable 3D nanoarchitecture was successfully fabricated for rapid, ultratrace DPV analysis of DNA hybridization. The structures and properties of AuNPs/GG1PD/MPA/Au were characterized. DFT calculation indicates that AuNPs had more specific interaction with internal cavities and terminal functional groups of the PD in the GG1PD material, and AuNPs decorated onto G1GPD was an efficient template to improve the electrocatalytic activity and chemical stabilization, which was employed to covalently immobilize thiol-functionalized single-stranded DNA as biorecognition element to form the DNA nanobiosensor. Different parameters like immersion times, contents, and pH were optimized and evaluated using $[Fe(CN)_6]^{3-/4-}$ as the redox probe. The fabricated nanobiosensing device with an optimized 3D nanostructural thin film resulted in a rapid, ultrasensitive, and label-free detection of DNA hybridization with a low LOD of 9.07×10^{-14} M. This work will be a promising way in the controllable 3D nanoarchitecture of the LBL-assembled metal nanoparticles-functionalized lower-generation PD thin films with two-dimensional layered nanomaterials as a core, ultrasensitive, and label-free nanobiosensing platform with a controllable 3D nanoarchitecture as novel DNA biodevice for the fast diagnosis of genetic disease and other biomedical applications in genopathy. In addition, applications of the structures, electrochemical properties, and gene biosensing of the LBL-assembled AuNPs-decorated lower-generation (GGn $\leq$ 3) graphene core PD with 3D nanostructure are also in progress.

■ ASSOCIATED CONTENT

Supporting Information

The Supporting Information is available free of charge on the ACS Publications website at DOI: 10.1021/acsami.8b03236.

Formulas (eqs S-1−5); ATR-FTIR spectra of bare Au and MPA/Au and SERS spectrum of GO (Figure S-1); height profile surface morphologies and AFM images of MPA layer with various immersion times (Figure S-2); CVs and Nyquist impedance of Au electrodes modified with different materials (Figure S-3); UV−vis spectra of different materials and characteristic peaks of Au $4f_{7/2}$ XPS spectra (Figure S-4); CVs of different electrodes at different v values (Figure S-6); plots of I_{pa} and I_{pc} vs $v^{1/2}$ at different electrodes (Figure S-7); plots of log I_{pa} and log I_{pc} vs log v at different electrodes (Figure S-8); Au−O anchor bond distances (d_{O-Au}) in angstrom (Table S-1); and the comparison of graphene nanocomposite materials for DNA biosensing (Table S-2) (PDF)

■ AUTHOR INFORMATION

Corresponding Authors

*E-mail: jkvare@gmail.com (K.J.).
*E-mail: dharumanudhay@yahoo.com (V.D.).
*E-mail: wenyangping1980@gmail.com (Y.W.).

ORCID

María Belén Camarada: 0000-0001-5408-3073
Huangxian Ju: 0000-0002-6741-5302
Yangping wen: 0000-0001-7047-4533

DOI: 10.1021/acsami.8b03236
ACS Appl. Mater. Interfaces 2018, 10, 21541−21555

Notes

The authors declare no competing financial interest.

■ ACKNOWLEDGMENTS

This study was financially supported by the Council of Scientific and Industrial Research (CSIR No. 03(1160)/10/EMR-II), DST INSPIRE (04/2015/000337), Govt. of India and Fondecyt Chile (1180023), Powered@NLHPC: This research was partially supported by the supercomputing infrastructure of the NLHPC (ECM-02) Outstanding Young Talent Program of Jiangxi Province (20171BCB23042), and National Natural Science Foundation of China (51662014).

■ REFERENCES

(1) Sassolas, A.; Leca-Bouvier, B. D.; Blum, L. J. DNA Biosensors and Microarrays. *Chem. Rev.* **2008**, *108*, 109−139.
(2) Park, J. Y.; Park, S. M. DNA Hybridization Sensors Based on Electrochemical Impedance Spectroscopy as a Detection Tool. *Sensors* **2009**, *9*, 9513−9532.
(3) Aoki, H. Electrochemical Label-Free Nucleotide Sensors. *Chem. Asian J.* **2015**, *10*, 2560−2573.
(4) Drummond, T. G.; Hill, M. G.; Barton, J. K. Electrochemical DNA Sensors. *Nat. Biotechnol.* **2003**, *21*, 1192−1199.
(5) Bonanni, A.; Del-Valle, M. Use of Nanomaterials for Impedimetric DNA Sensors. *Anal. Chim. Acta* **2010**, *678*, 7−17.
(6) Heerema, S. J.; Dekker, C. S. Graphene Nanodevices for DNA Sequencing. *Nat. Nanotechnol.* **2016**, *11*, 127−131.
(7) Cai, B.; Wang, S.; Huang, L.; Ning, Y.; Zhang, Z.; Zhang, G.-J. Ultrasensitive Label-Free Detection of PNAÀDNA Hybridization by Reduced Graphene Oxide Field-Effect Transistor Biosensor. *ACS Nano* **2014**, *8*, 2632−2638.
(8) Loan, P. T.; Zhang, W.; Lin, C. T.; Wei, K. H.; Li, L. J.; Chen, C. H. P. Graphene/MoS_2 Heterostructures for Ultrasensitive Detection of DNA Hybridization. *Adv. Mater.* **2014**, *26*, 4838−4844.
(9) Jayakumar, K.; Camarada, M. B.; Dharuman, V.; Ju, H.; Dey, R. S.; Wen, Y. One-Step Coelectrodeposition-Assisted Layer-by-Layer Assembly of Gold Nanoparticles and Reduced Graphene Oxide and its Self-Healing Three-Dimensional Nanohybrid for an Ultrasensitive DNA Sensor. *Nanoscale* **2018**, *10*, 2658.
(10) Wu, L.; Xiong, E.; Zhang, X.; Zhang, X.; Chen, J. Nanomaterials as Signal Amplification Elements in DNA-Based Electrochemical Sensing. *Nano Today* **2014**, *9*, 197−211.
(11) Wu, S.; He, Q.; Tan, C.; Wang, Y.; Zhang, H. Graphene-Based Electrochemical Sensors. *Small* **2013**, *9*, 1160−1172.
(12) Tiwari, J. N.; Vij, V.; Kemp, K. C.; Kim, K. S. Engineered Carbon-Nanomaterial-Based Electrochemical Sensors for Biomolecules. *ACS Nano* **2016**, *10*, 46−80.
(13) Li, D.; Zhang, W.; Yu, X.; Wang, Z.; Su, Z.; Wei, G. When Biomolecules Meet Graphene: From Molecular Level Interactions to Material Design and Applications. *Nanoscale* **2016**, *8*, 19491−19509.
(14) Yu, X.; Zhang, W.; Zhang, P.; Siu, Z. Fabrication Technologies and Sensing Applications of Graphene-Based Composite Films: Advances and Challenges. *Biosens. Bioelectron.* **2017**, *89*, 72−84.
(15) Guo, Y.; Guo, Y.; Dong, C. Ultrasensitive and Label-Free Electrochemical DNA Biosensor Based on Water-Soluble Electroactive Dye Azophloxine-Functionalized Graphene Nanosheets. *Electrochem. Acta* **2013**, *113*, 69−76.
(16) Yuan, Y.; Gou, X.; Yuan, R.; Chaia, Y.; Zhuo, Y.; Ye, X.; Gan, X. Graphene-Promoted 3,4,9,10-Perylenetetracarboxylic Acid Nanocomposite as Redox Probe in Label-Free Electrochemical Aptasensor. *Biosens. Bioelectron.* **2011**, *30*, 123−127.
(17) Chen, M.; Hou, C.; Huo, D.; Bao, J.; Fa, H.; Shen, C. An Electrochemical DNA Biosensor Based on Nitrogen-Doped Graphene/Au Nanoparticles for Human Multidrug Resistance Gene Detection. *Biosens. Bioelectron.* **2016**, *85*, 684−691.
(18) Bahadır, E. B.; Sezgintürk, M. K. Poly(amidoamine) (PAMAM): An emerging material for electrochemical bio(sensing) applications. *Talanta* **2016**, *148*, 427−438.
(19) Liu, H.; Wang, H.; Yang, W.; Cheng, Y. Disulfide Cross-Linked Low Generation Dendrimers with High Gene Transfection Efficacy, Low Cytotoxicity, and Low Cost. *J. Am. Chem. Soc.* **2012**, *134*, 17680−17687.
(20) Zhu, N.; Gao, H.; Xu, Q.; Lin, Y.; Su, L.; Mao, L. Sensitive Impedimetric DNA Biosensor with Poly(amidoamine) Dendrimer Covalently Attached onto Carbon Nanotube Electronic Transducers as the Tether for Surface Confinement of Probe DNA. *Biosens. Bioelectron.* **2010**, *25*, 1498−1503.
(21) Hasanzadeh, M.; Shadjou, N.; Eskandani, M.; Soleymani, J.; Jafaria, F.; Guardia, M. Dendrimer-Encapsulated and Cored Metal Nanoparticles for Electrochemical Nanobiosensing. *TrAC, Trends Anal. Chem.* **2014**, *53*, 137−149.
(22) Tang, D.; Tang, J.; Su, B.; Chen, G. Gold Nanoparticles-Decorated Amine-Terminated Poly(amidoamine) Dendrimer for Sensitive Electrochemical Immunoassay of Brevetoxins in Food Samples. *Biosens. Bioelectron.* **2011**, *26*, 2090−2096.
(23) Dietrich, S.; Schulze, S.; Hietschold, M.; Lang, H. Au Nanoparticles Stabilised by PEGylated Low Generation PAMAM Dendrimers: Design, Characterisation and Properties. *J. Colloid Interfaces Sci.* **2011**, *359*, 454−460.
(24) Hummers, W. S.; Offeman, R. E. Preparation of Graphitic Oxide. *J. Am. Chem. Soc.* **1958**, *80*, 1339.
(25) Jayakumar, K.; Rajesh, R.; Dharuman, V.; Venkatasan, R.; Hahn, J. H.; Pandian, S. K. Gold Nanoparticle Decorated Graphene Core First Generation PAMAM Dendrimer for Label Free Electrochemical DNA Hybridization Sensing. *Biosens. Bioelectron.* **2012**, *31*, 406−412.
(26) Frens, G. Controlled Nucleation for Regulation of Particle-Size in Monodisperse Gold Suspensions. *Nat. Phys. Sci.* **1973**, *241*, 20−22.
(27) Becke, A. D. Density-Functional Thermochemistry. III. The Role of Exact Exchange. *J. Chem. Phys.* **1993**, *98*, 5648−5652.
(28) Lee, C.; Yang, W.; Parr, R. G. Development of the Colle-Salvetti Correlation-Energy Formula into a Functional of the Electron Density. *Phys. Rev. B* **1988**, *37*, 785−789.
(29) Stephens, J. P.; Devlin, F. J.; Chabalowski, C. F.; Frisch, M. J. Ab Initio Calculation of Vibrational Absorption and Circular Dichroism Spectra Using Density Functional Force Fields. *J. Phys. Chem.* **1994**, *98*, 11623−11627.
(30) Hay, P. J.; Wadt, W. R. Ab Initio Effective Core Potentials for Molecular Calculations. Potentials for the Transition Metal Atoms Sc to Hg. *J. Chem. Phys.* **1985**, *82*, 270−283.
(31) Reed, A. E.; Weinstock, R. B.; Weinhold, F. Natural Population Analysis. *J. Chem. Phys.* **1985**, *83*, 735−746.
(32) Boys, S. F.; Bernardi, F. The Calculation of Small Molecular Interactions by the Differences of Separate Total Energies. Some Procedures with Reduced Errors. *Mol. Phys.* **1970**, *19*, 553−566.
(33) Cross, J. P.; Lauz, M.; Badger, P. D.; Petoud, S. Polymetallic Lanthanide Complexes with PAMAM-Naphthalimide Dendritic Ligands: Luminescent Lanthanide Complexes Formed in Solution. *J. Am. Chem. Soc.* **2004**, *126*, 16278−16279.
(34) Ataka, K.; Heberle, J. Functional Vibrational Spectroscopy of a Cytochrome C Monolayer: SEIDAS Probes the Interaction with Different Surface-Modified Electrodes. *J. Am. Chem. Soc.* **2004**, *126*, 9445−9457.
(35) Eigler, S.; Dotzer, C.; Hirsch, A. Visualization of Defect Densities in Reduced Graphene Oxide. *Carbon* **2012**, *50*, 3666−3673.
(36) Goncalves, G.; Marques, P. A. A. P.; Granaderio, C. M.; Nogueira, H. I. S.; Singh, M. K.; Grácio, J. Surface Modification of Graphene Nanosheets with Gold Nanoparticles: The Role of Oxygen Moieties at Graphene Surface on Gold Nucleation and Growth. *Chem. Mater.* **2009**, *21*, 4796−4802.
(37) Xie, W.; Weng, L. T.; Ng, K.; Chan, C.; Chan, C. M. Clean Graphene Surface Through High Temperature Annealing. *Carbon* **2015**, *94*, 740−748.

DOI: 10.1021/acsami.8b03236
ACS Appl. Mater. Interfaces 2018, 10, 21541−21555

(38) Kryachko, E. S.; Remacle, F. Complexes of DNA Bases and Gold Clusters Au3 and Au4 Involving Nonconventional N-H Au Hydrogen Bonding. *Nano Lett.* **2005**, *5*, 735−739.
(39) Cançado, L. G.; Jorio, A.; Pimenta, M. A. Measuring the Absolute Raman Cross Section of Nanographites as a Function of Laser Energy and Crystallite Size. *Phys. Rev. B* **2007**, *76*, No. 064304.
(40) Yu, Y.-J.; Zhao, Y.; Ryu, S.; Brus, L. E.; Kim, K. S.; Kim, P. Tuning the Graphene Work Function by Electric Field Effect. *Nano Lett.* **2009**, *9*, 3430−3434.
(41) Tung, V. C.; Allen, M. J.; Yang, Y.; Kaner, R. B. High-Throughput Solution Processing of Large-Scale Graphene. *Nat. Nanotechnol.* **2009**, *4*, 25−29.
(42) Gao, W.; Alemany, L. B.; Ci, L.; Ajayan, P. M. New Insights into the Structure and Reduction of Graphite Oxide. *Nat. Chem.* **2009**, *1*, 403−408.
(43) Khandelwal, M.; Kumar, A. One-Pot Environmentally Friendly Amino Acid Mediated Synthesis of N-Doped Graphene-Silver Nanocomposites with an Enhanced Multifunctional Behavior. *Dalton Trans.* **2016**, *45*, 5180−5195.
(44) Giovannetti, G.; Khomyakov, P. A.; Brocks, G.; Karpan, V. M.; Brink, J. V.; Kelly, P. J. Doping Graphene with Metal Contacts. *Phys. Rev. Lett.* **2008**, *101*, No. 026803.
(45) Asahi, R.; Morikawa, T.; Ohwaki, T.; Aoki, A.; Taga, T. Visible-Light Photocatalysis in Nitrogen-Doped Titanium Oxides. *Science* **2001**, *293*, 269−271.
(46) Kryachko, E. S.; Remacle, F. Complexes of DNA Bases and Watson-Crick Base Pairs with Small Neutral Gold Clusters. *J. Phys. Chem. B* **2005**, *109*, 22746−22757.
(47) Bard, A. J.; Faulkner, L. R. *Electrochemical Methods: Fundamentals and Applications*, 2nd ed.; John Wiley & Sons: New York, 2001.
(48) Lei, W.; Si, W. M.; Hao, Q. L.; Han, Z.; Zhang, Y. H.; Xia, M. Z. Preparation and Characterization of Gold Nanoparticles Decorated on Graphene Oxide@Polydopamine Composite: Application for Sensitive and Low Potential Detection of Catechol. *Sens. Actuators, A* **2015**, *212*, 207−213.
(49) Zhang, Z.; Zhang, J.; Zhang, H.; Xu, J.; Wen, Y.; Ding, W. Characterization of PEDOT: PSS-Reduced Graphene Oxide@Pd Composite Electrode and its Application in Voltammetric Determination of Vitamin K_3. *J. Electroanal. Chem.* **2016**, *775*, 258−266.
(50) Pheeney, C. G.; Barton, J. K. DNA Electrochemistry with Tethered Methylene Blue. *Langmuir* **2012**, *28*, 7063−7070.
(51) Evtyugin, G. A.; Stoikova, E. E. Electrochemical Biosensors Based on Dendrimers. *J. Anal. Chem.* **2015**, *70*, 517−534.
(52) Wei, M. Y.; Guo, L. H.; Famouri, P. Label-Free Electrochemical Measurement of Protein Tyrosine Kinase Activity and Inhibition Based on Electro-Catalyzed Tyrosine Signaling. *Microchim. Acta* **2011**, *172*, 247−260.
(53) Wang, J.; Rivas, G.; Cai, X.; Palecek, E.; Nielsen, P.; Shiraishi, H.; Dontha, N.; Luo, D.; Parrado, C.; Chicharro, M.; Farias, P. A. M.; Valera, F. S.; Grant, D. H.; Ozsoz, M.; Flair, M. N. DNA Electrochemical Biosensors for Environmental Monitoring, A Review. *Anal. Chim. Acta* **1997**, *347*, 1−8.
(54) Teles, F. R. R.; Fonseca, L. P. Trends in DNA Biosensors. *Talanta* **2008**, *77*, 606−623.
(55) Liu, J.; Liu, J.; Yang, L.; Chen, X.; Zhang, M.; Meng, F.; Luo, T.; Li, M. Nanomaterial-Assisted Signal Enhancement of Hybridization for DNA Biosensors, a Review. *Sensors* **2009**, *9*, 7343−7364.
(56) Bonanni, A.; Pividori, M. I.; del Valle, M. DNA Polymorphism Sensitive Impedimetric Detection on Gold-Nanoislands Modified Electrodes. *Talanta* **2015**, *136*, 95−101.

DOI: 10.1021/acsami.8b03236
ACS Appl. Mater. Interfaces 2018, 10, 21541−21555